Physics of Fluids

Instability of large-scale riverbed patterns

Cite as: Phys. Fluids **33**, 015109 (2021); https://doi.org/10.1063/5.0035893
Submitted: 01 November 2020 . Accepted: 12 December 2020 . Published Online: 05 January 2021

Sk Zeeshan Ali, and Subhasish Dey

View Online Export Citation CrossMark

ARTICLES YOU MAY BE INTERESTED IN

The law of the wall: A new perspective
Physics of Fluids **32**, 121401 (2020); https://doi.org/10.1063/5.0036387

Fluvial instabilities
Physics of Fluids **32**, 061301 (2020); https://doi.org/10.1063/5.0010038

Hydrodynamic instability of free river bars
Physics of Fluids **33**, 045105 (2021); https://doi.org/10.1063/5.0045530

Physics of Fluids
SPECIAL TOPIC: Tribute to
Frank M. White on his 88th Anniversary
SUBMIT TODAY!

AIP Publishing

© 2021 Author(s).

Physics of Fluids ARTICLE scitation.org/journal/phf

Instability of large-scale riverbed patterns

Cite as: Phys. Fluids 33, 015109 (2021); doi: 10.1063/5.0035893
Submitted: 1 November 2020 • Accepted: 12 December 2020 •
Published Online: 5 January 2021

View Online Export Citation CrossMark

Sk Zeeshan Ali[1,a] and Subhasish Dey[2,3,b]

AFFILIATIONS

[1] Department of Civil Engineering, Indian Institute of Technology Hyderabad, Hyderabad, Telangana 502285, India
[2] Department of Civil Engineering, Indian Institute of Technology Kharagpur, Kharagpur, West Bengal 721302, India
[3] Department of Hydraulic Engineering, State Key Laboratory of Hydro-Science and Engineering, Tsinghua University, Beijing 100084, China

[a] **Author to whom correspondence should be addressed:** zeeshan@ce.iith.ac.in
[b] sdey@iitkgp.ac.in

ABSTRACT

In this paper, we explore the instability of large-scale riverbed patterns, performing a linear stability analysis of a zero-pressure gradient free-surface flow in a wide straight channel with an erodible bed. The local depth-averaged turbulence state is governed by two key parameters: namely, the turbulent kinetic energy (TKE) and its dissipation rate. A depth-averaged flow model coupled with the transport equations of the TKE and its dissipation rate and the particle transport model are developed to examine the formation of large-scale patterns. Both the modes of particle transport as bedload and suspended load are considered herein, allowing for the extension of the conventional theories to cover from hydraulically smooth to transitional flow regimes. The classical Exner equation of the bed evolution is modified in the presence of suspended particles, whose concentration is coupled with the steady-state advection–diffusion equation. Applying a standard linearization technique, the periodic perturbations in both streamwise and spanwise directions are imposed on the bed to find the dispersion relationship. The stability maps for the growth rate of large-scale patterns are obtained as a function of streamwise and spanwise wavenumbers and of key parameters associated with the flow and particles.

Published under license by AIP Publishing. https://doi.org/10.1063/5.0035893

I. INTRODUCTION

The instability of riverbed patterns has fascinated researchers for more than 50 years.[1–7] The instability primarily originates from a subtle interaction between a carrier fluid and a loose erodible bed at their interface. Riverbed patterns are grouped into three major classes in terms of their characteristic streamwise wavelength, such as small-scale, intermediate-scale, and large-scale patterns. The small-scale patterns include ripples, whose characteristic wavelength is proportional to the particle size. The intermediate-scale patterns comprise dunes and antidunes, where the characteristic wavelength scales with the flow depth. In addition, the large-scale patterns consist of bars, whose typical wavelength is of the order of a channel width.

Over the decades, researchers made significant progress in understanding the mechanics of the formation of riverbed patterns from the experimental evidence and theoretical approaches (see the state-of-the-art reviews in Refs. 6 and 7). Kennedy[1] and Engelund and Fredsøe[2] compiled the studies on the formation and the instability of riverbed patterns. Additionally, Southard[3] compiled ample experimental and field observations to review the instability of riverbed patterns from a broader perspective. In particular, the instability of riverbed patterns has largely been studied from an analytical perspective.[1,2,4,6,7] The analytical approach is based on some fundamental concepts of instability that eventually gave rise to three distinct modeling strategies, such as the potential flow model,[1] shallow water model,[8,9] and rotational flow model.[10–14] Since the potential flow model is not capable of producing fluid-induced shear stress at the bed, a phase lag distance is commonly introduced while creating the instability. However, the shallow water model can effectively resolve the drawback of the potential flow model because it takes into account the frictional effects. In addition, the rotational flow model offers a satisfactory estimate of the bed shear stress that produces instability. Specifically, two separate patterns of instability were identified in a hydraulically rough flow regime.[10] The first pattern corresponds to ripples (wavelength scales with the bed roughness height) and the second is related to dunes (wavelength scales with the flow depth). With regard to the formation of riverbed

patterns in the framework of the shallow water model, the depth-averaged continuity and momentum equations were linearized to seek the stable and unstable zones.[8,9] Employing a rotational flow model, the linear stability analysis of two-dimensional riverbed patterns in a conventionally rough flow regime[11] was extended to cover smooth and transitional flow regimes.[13] Moreover, the formation of both two- and three-dimensional riverbed patterns was analyzed by using the rotational flow model coupled with the bedload transport model.[11–14]

The driving mechanism of the instability of riverbed patterns was reported to be the phase lag between the particle flux and the bed shear stress.[6] In the near-bed flow zone, the phase lag depicts a considerable variation.[11] In fact, several relevant factors control the phase lag; for instance, frictional effects, presence of suspended particles, particle inertia, and gravity.[2,7] Colombini[11] pointed out that in a bedload dominated channel flow, the fluid stress perturbations causing the instability should be determined at the top of the saltation layer (also called bedload layer) within which the bedload transport prevails. This subtle modification has been proven to be a key step in revisiting the linear theory of riverbed patterns.[11]

Here, we specifically focus on the instability of large-scale riverbed patterns.[15] Extensive survey on this topic was reviewed recently by Crosato and Mosselman.[16] The current state-of-the-art of the instability of large-scale riverbed patterns offers an enriched understanding of the evolutions of patterns and the relevant parameters that govern their stability. However, there remain a few key concerns with regard to the instability mechanism from an analytical perspective. For intense bed shear stress, the fluid flow produces a massive amount of suspended particles, which have a positive contribution to the phase lag. In fact, the peak transport of suspended particles occurs downstream of the location of the peak bed shear stress.[2] When the suspended load dominates the bedload, the positive contribution from suspended particles exceeds the negative contribution from frictional effects. Moreover, the presence of suspended particles can substantially alter the instability mechanism of bars.[17,18] The existing literature does not describe how the evolution of large-scale riverbed patterns is sensitive to flow regimes. Although the effects of flow regimes are well-known for small- and intermediate-scale patterns,[13] current analyses of three-dimensional large-scale patterns are mostly limited to a conventionally rough flow regime. In brief, the existing analytical models of large-scale patterns are incapable of incorporating both the effects of flow regimes and particle suspension.

In the present formulation, we develop a model that addresses each of the above issues. In fact, these issues can be effectively resolved by refining the conventional way of modeling the instability of large-scale riverbed patterns. In order to widely apply the present theory, several numerical experiments are conducted wherever feasible to capture the response of riverbed patterns to relevant parameters. The mathematical formulation presents a linear stability theory of turbulent flow over an erodible bed. Unlike the existing models of linear stability of large-scale riverbed patterns, this study models the instability by introducing the transport equations of the turbulent kinetic energy (TKE) and its dissipation rate. Furthermore, the shear stress that drives the particle transport is considered at the top of the saltation layer. Both the bedload and suspended load are considered to be the modes of particle transport. The classical Exner equation of the bed evolution is revised by considering the effects of particle suspension. In Sec. II, it is shown that the mathematical analysis is not only applicable to a hydraulically rough flow regime but also stretchable to smooth and transitional flow regimes.

The rest of this paper is arranged as follows: In Secs. II and III, the mathematical formulations for the flow and particle transport are presented, respectively. The set of equations is linearized in Sec. IV. The model results are discussed in Sec. V. Finally, conclusions are drawn in Sec. VI.

II. MATHEMATICAL FORMULATION: FLOW MODEL

We consider a zero-pressure gradient free-surface flow of an incompressible fluid in a wide straight channel. The flow is turbulent. Hereafter, a star superscript represents a dimensional variable. With respect to a Cartesian coordinate system (x^*, y^*, z^*), where x^*, y^*, and z^* represent streamwise, spanwise, and vertical distances, respectively (Fig. 1), the flow domain at a given time t^* is confined to two wavy surfaces $z^* = R^*(x^*, y^*, t^*)$ and $z^* = R^*(x^*, y^*, t^*) + D^*(x^*, y^*, t^*)$. Here, D^* is the local flow depth. The former wavy surface is set at a reference level R^*, where the flow velocity obtained from the classical logarithmic law ceases.

To make the variables dimensionless, we consider the triplet formed by the undisturbed flow depth D_0^*, depth-averaged undisturbed streamwise velocity U_0^*, and mass density of fluid ρ_f. Henceforth, the variable with a subscript "0" represents the undisturbed state. We introduce a set of dimensionless variables and the flow Froude number Fr corresponding to the undisturbed state as

$$(x, y, z) = \frac{(x^*, y^*, z^*)}{D_0^*}, \ (R, D) = \frac{(R^*, D^*)}{D_0^*}, \ \boldsymbol{U} = \frac{\boldsymbol{U}^*}{U_0^*}, \\ \boldsymbol{T} = \frac{\boldsymbol{T}^*}{\rho_f U_0^{*2}}, \text{ and } Fr = \frac{U_0^*}{(gD_0^*)^{1/2}}, \tag{1}$$

where $\boldsymbol{U} = (U, V)$ is the local depth-averaged velocity vector, $\boldsymbol{T}$ is the stress tensor, and g is the gravitational acceleration. The governing equations of fluid dynamics pertaining to the physical system, as shown in Fig. 1, can be readily derived by depth-averaging the time-averaged flow equations subject to suitable boundary conditions. It is pertinent to mention that the depth-averaged assumptions are justified in investigating the instability of large-scale patterns.[15]

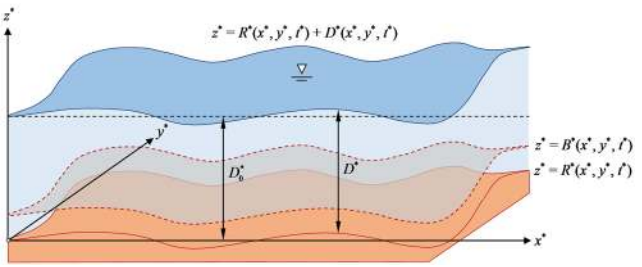

FIG. 1. Conceptual sketch of the flow model. The reference level and the free surface are denoted by $z^* = R^*(x^*, y^*, t^*)$ and $z^* = R^*(x^*, y^*, t^*) + D^*(x^*, y^*, t^*)$, respectively. The D_0^* represents the undisturbed flow depth. The wavy surface with a dashed line, defined by $z^* = B^*(x^*, y^*, t^*)$, indicates the top edge of the saltation layer.

Published under license by AIP Publishing

For a steady flow, the depth-averaged continuity and momentum equations read[19]

$$\frac{\partial}{\partial x}(DU) + \frac{\partial}{\partial y}(DV) = 0, \tag{2}$$

$$U\frac{\partial U}{\partial x} + V\frac{\partial U}{\partial y} + \frac{1}{Fr^2}\frac{\partial}{\partial x}(D+R) - \frac{1}{D}\frac{\partial}{\partial x}(DT_{xx}) - \frac{1}{D}\frac{\partial}{\partial y}(DT_{xy}) - Q_{xx} - Q_{xy} + \frac{T_{bx}}{D} = 0, \tag{3}$$

$$U\frac{\partial V}{\partial x} + V\frac{\partial V}{\partial y} + \frac{1}{Fr^2}\frac{\partial}{\partial y}(D+R) - \frac{1}{D}\frac{\partial}{\partial x}(DT_{yx}) - \frac{1}{D}\frac{\partial}{\partial y}(DT_{yy}) - Q_{yx} - Q_{yy} + \frac{T_{by}}{D} = 0, \tag{4}$$

where $\boldsymbol{Q}$ includes the dispersion terms and $\boldsymbol{T}_b = (T_{bx}, T_{by})$ is the local bed shear stress vector. In order to close the above system, the turbulent stresses are modeled by employing the K–ε turbulence closure model that incorporates the eddy viscosity ν_T^* in the model formulation. Consequently, the turbulent stress tensor T_{ij} takes the form of

$$T_{ij} = \nu_T\left(\frac{\partial U_i}{\partial x_j} + \frac{\partial U_j}{\partial x_i}\right) - \frac{2}{3}\delta_{ij}K, \tag{5}$$

where δ_{ij} is the Kronecker delta function. In analogy with the standard K–ε turbulence model, it is considered herein that the local depth-averaged turbulence state is driven by two parameters, such as the TKE, K, and its dissipation rate, ε. It is worth noting that although the K–ε turbulence model is based on the isotropic assumption of eddy viscosity, this specific assumption may have little influence on the marginal stability of large-scale patterns.[19] Based on the dimensional ground, the eddy viscosity ν_T is linked with these parameters via a proportionality constant c_μ as follows:

$$\nu_T = c_\mu\frac{K^2}{\varepsilon}. \tag{6}$$

In the above, the proportionality constant c_μ is considered to be 0.01.[20] The turbulence parameters K and ε satisfy the following transport equations:[19]

$$U\frac{\partial K}{\partial x} + V\frac{\partial K}{\partial y} = \frac{\partial}{\partial x}\left(\frac{\nu_T}{\sigma_K}\frac{\partial K}{\partial x}\right) + \frac{\partial}{\partial y}\left(\frac{\nu_T}{\sigma_K}\frac{\partial K}{\partial y}\right) + P_H + P_{KV} - \varepsilon, \tag{7}$$

$$U\frac{\partial \varepsilon}{\partial x} + V\frac{\partial \varepsilon}{\partial y} = \frac{\partial}{\partial x}\left(\frac{\nu_T}{\sigma_\varepsilon}\frac{\partial \varepsilon}{\partial x}\right) + \frac{\partial}{\partial y}\left(\frac{\nu_T}{\sigma_\varepsilon}\frac{\partial \varepsilon}{\partial y}\right) + c_{1\varepsilon}\frac{\varepsilon}{K}P_H + P_{\varepsilon V} - c_{2\varepsilon}\frac{\varepsilon^2}{K}, \tag{8}$$

where P_H is the production rate of K resulting from interactions of turbulent stresses with gradients of time-averaged horizontal velocity components on the xy plane, P_{KV} and $P_{\varepsilon V}$ are the production rates of K and ε, respectively, arising from the vertical velocity gradients in the near-bed flow zone, and $(c_{1\varepsilon}, c_{2\varepsilon}, \sigma_K, \sigma_\varepsilon)$ is a set of coefficients in the standard K–ε turbulence model. Characteristic values of these constants are taken as $c_{1\varepsilon} = 1.44$, $c_{2\varepsilon} = 1.92$, $\sigma_K = 1$, and $\sigma_\varepsilon = 1.22$.[20] The P_H, P_{KV}, and $P_{\varepsilon V}$ are formulated as follows:[19]

$$P_H = \nu_T\left[2\left(\frac{\partial U}{\partial x}\right)^2 + 2\left(\frac{\partial V}{\partial y}\right)^2 + \left(\frac{\partial U}{\partial y} + \frac{\partial V}{\partial x}\right)^2\right],$$
$$P_{KV} = \frac{1}{C_f^{1/2}}\frac{u_f^3}{D}, \text{ and } P_{\varepsilon V} = \frac{c_{2\varepsilon}c_\mu^{1/2}}{a_0^{1/2}C_f^{3/4}}\frac{u_f^4}{D^2}, \tag{9}$$

where the newly introduced dimensionless variables are the conductance coefficient C_f and the friction velocity u_f. Note that a_0 represents the eddy viscosity ν_T^* scaled by the term $u_f^* D^*$. Furthermore, u_f can be expressed as

$$u_f = |\boldsymbol{T}_b|^{1/2} = [C_f(U^2 + V^2)]^{1/2}. \tag{10}$$

The local bed shear stress vector is formulated as a function of dynamic pressure via the conductance coefficient. Therefore, the $\boldsymbol{T}_b$ reads

$$\boldsymbol{T}_b = (T_{bx}, T_{by}) = C_f(U^2 + V^2)^{1/2}(U, V). \tag{11}$$

It has been revealed that the comparison of theoretical stability analysis with measurements requires the estimation of shear stress that acts on a plane bed.[15] It turns out that the contributions from form-drag and channel sidewalls to the local bed shear stress vector are vanishingly small. This suggests that the local bed shear stress is to be modeled based on a quasi-zero-pressure gradient flow assumption. The conductance coefficient C_f for a plane bed follows the well-recognized Colebrook–White equation, since this has an excellent agreement with a large corpus of experimental and field observations.[21] Furthermore, the C_f can be related to Darcy–Weisbach friction factor λ_b as

$$\frac{1}{(8C_f)^{1/2}} = \frac{1}{\lambda_b^{1/2}} = -0.86\ln\left(\frac{k_s^*}{a_r D^*} + \frac{a_s}{Re}\lambda_b^{-1/2}\right) \text{ with } Re = \frac{4U_0^* D_0^*}{\upsilon}, \tag{12}$$

where k_s^* is the bed roughness height, Re is the flow Reynolds number, and υ is the coefficient of kinematic viscosity of the fluid. In the above, the constants a_r and a_s, being representative of the hydraulically rough and smooth flow regimes, are considered to be 14.8 and 2.51, respectively.[22] Note that although the above formulation is strictly applicable to the transitional flow regime, it is stretchable to smooth and rough flow regimes with a promising accuracy. In this context, it is worth mentioning that the flow regimes are classified according to some characteristic ranges of roughness Reynolds number Re_k. Therefore, we set

$$Re_k = \frac{u_f^* k_s^*}{\upsilon} = Re\left(\frac{\lambda_b}{8}\right)^{1/2} k_s, \tag{13}$$

where the characteristic range of the transitional flow regime corresponds to $5 < Re_k < 70$.

The effects of the dispersion terms in Eqs. (3) and (4) are similar to those of turbulent stresses because both signify gradients of the momentum transport. It has been evidenced that the effects of dispersion terms in the depth-averaged equations are important when secondary currents are no way negligible. Under such a circumstance, the importance of dispersion terms and turbulent stresses

Published under license by AIP Publishing

are of the same order of magnitude (at least quantitatively).[19] Computations and experimental observations have suggested that in the depth-averaged formulation, the effects of dispersion terms can be incorporated indirectly by enhancing the magnitude of the eddy viscosity. In the present formulation, this may be achieved by considering a larger value of a_0 [see Eq. (9)] than its traditional value. The depth-averaged undisturbed eddy viscosity ν_{T0} conventionally follows $\nu_{T0} = \kappa u_{f0}/6$, where κ is the von Kármán coefficient (= 0.41). This suggests that a_0 is of the order of 0.1. Laboratory experiments in wide channels reported $a_0 \approx 0.15$,[19] while field measurements in weak meandering rivers with moderate side-wall irregularities have evidenced $a_0 \approx 0.6$.[19] In the present analysis, the a_0 is considered to be 0.375 as an average value.

To close the system, additional formulation for the TKE is required. The TKE is expressed as $k^*(z^*) = (\sigma_1^{*2} + \sigma_2^{*2} + \sigma_3^{*2})/2$, where σ_i^* is the ith turbulence intensity. A large set of experimental data from the available literature suggested that the σ_i^* scaled by the friction velocity u_f^* follows an exponential distribution as

$$\frac{\sigma_i^*}{u_f^*} = M_i \exp\left(-N_i \frac{z-R}{D}\right), \tag{14}$$

where M_i and N_i are the empirical constants. For instance, Nezu[23] reported M_i and N_i (i = 1–3) as $M_1 = 2.3$, $M_2 = 1.63$, $M_3 = 1.27$, and $N_1 = N_2 = N_3 = 1$. The above relationship has been found to provide a rational estimation of the TKE in open-channel flows with both rigid and mobile beds.[24,25] In fact, Eq. (14) was proposed using the turbulence closure model with an assumption of local equilibrium of TKE, where the production of TKE is balanced by its dissipation rate. Nikora and Goring[26] proposed a logarithmic scaling for the ith turbulence intensity squared in the equilibrium layer by applying parameterization of the velocity spectra. They revised Eq. (14) as

$$\left(\frac{\sigma_i^*}{u_f^*}\right)^2 = M_i - N_i \ln\left(\frac{z-R}{D}\right), \tag{15}$$

where the constants were obtained as $M_1 = 1.90$, $M_2 = 1.19$, $M_3 = 0.59$, $N_1 = 1.32$, $N_2 = 0.49$, and $N_3 = 0.22$.

Figure 2 shows the experimental data plots of dimensionless TKE, k^*/u_f^{*2}, as a function of dimensionless vertical distance, $(z - R)/D$. The experimental data correspond to three different flow conditions, namely, high weakly mobile-bed, medium fixed-bed, and low fixed-bed flows, as obtained by Nikora and Goring.[27] In addition, logarithmic scaling of Nikora and Goring,[26] Eq. (15) (shown by the dotted line in Fig. 2), together with the empirical formula of Nezu,[23] Eq. (14), as a reference (shown by the dashed line in Fig. 2), is plotted. It is worth mentioning that both the exponential and logarithmic scaling relationships could not replicate the behavior of TKE covering the entire flow depth. The underlying reason is attributed to the local energy equilibrium assumption, which fails very close to and away from the channel bed. In addition, these formulations do not reflect the effects of relative roughness d_r (ratio of particle size d^* to undisturbed flow depth D_0^*) and flow Reynolds number, which can significantly alter the fitted parameters in Eqs. (14) and (15). Therefore, both the scaling relationships require improvement in order to satisfactorily capture the experimental data. In this study, an exponential scaling for the TKE is considered over the entire flow depth. Therefore, the dimensionless

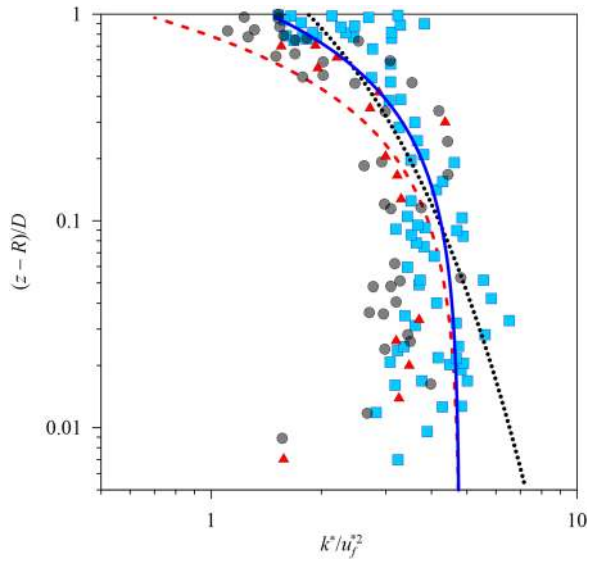

FIG. 2. Vertical distribution of dimensionless TKE. Experimental data of high weakly mobile-bed (squares), medium fixed-bed (circles), and low fixed-bed (triangles) flows are taken from the work of Nikora and Goring.[27] Dotted line—prediction of Nikora and Goring, [26] dashed line—empirical formula of Nezu[23] for a rigid-bed flow, and solid line—exponential scaling given by Eq. (16).

TKE takes the form of

$$\frac{k^*}{u_f^{*2}} = A_K \exp\left(-A_L \frac{z-R}{D}\right), \tag{16}$$

where A_K and A_L are constants. The advantage of Eq. (16) over the logarithmic scaling [Eq. (15)] is that unlike the logarithmic scaling, Eq. (16) does not invite singularity at the reference level ($z = R$). In the light of experimental observations (Fig. 2), it is found that Eq. (16) (shown by the solid line in Fig. 2), with constants $A_K = 4.78$ and $A_L = 1.2$, acts as a surrogate for the logarithmic scaling in the range $0.1 < (z - R)/D < 1$, whereas it provides an improvement over the prediction of Nikora and Goring[26] for $(z - R)/D < 0.1$. Note that the logarithmic scaling is not capable of addressing the near-bed damping of TKE. However, experimental measurements have evidenced that in the near-bed flow zone, particularly for $(z - R)/D < 0.1$, the values of TKE for weakly mobile-bed flow are larger than those for fixed-bed flow.[27] Furthermore, in Fig. 2, the comparison shows that the proposed exponential scaling for $(z - R)/D < 0.1$ corroborates the empirical formula of Nezu.[23] It is worth noting that the prescribed values of A_K and A_L, corresponding to a high weakly mobile-bed, medium fixed-bed, and low fixed-bed flows, can be considered to be of general validity as they comply with the measurements, providing a direct estimation of the depth-averaged TKE for the undisturbed state. However, with regard to the linear stability analysis, it was found that a deviation (within ±50%) from the prescribed values of A_K and A_L has little influence on the marginal stability curves. Integrating Eq. (16), the depth-averaged TKE can be obtained as

$$K = C_f \frac{A_K}{A_L}[1 - \exp(-A_L)], \tag{17}$$

Published under license by AIP Publishing

wherein the TKE is directly linked with the conductance coefficient and hence with the friction factor. The above formulation is useful to determine the depth-averaged TKE for the undisturbed state.

III. MATHEMATICAL FORMULATION: PARTICLE TRANSPORT MODEL

The granular bed is considered to be formed by uniform particles. Under this circumstance, when the bed shear stress exceeds its threshold value for the initiation of particle motion, particles are transported as bedload in rolling, sliding, and saltating modes within a thin fluid layer called the saltation layer.[22] In Fig. 1, the top edge of the saltation layer is denoted by B^*. However, when the bed shear stress is intensified, quite a few particles are entrained beyond the saltation layer and are transported as suspended load in the suspension layer. In this situation, both the bedload and suspended load transports prevail and the bed evolution is governed by their combined effects. To formulate the particle transport model, we allow both the bedload and suspended load transports, as sketched in Fig. 3(a). Below, we briefly discuss their role toward the instability mechanism.

In Fig. 3(a), the reference level R^* is set slightly below the summit of the bed particles. The datum $z^* = 0$ is conventionally positioned at a distance of $d^*/4$ below the summit of the bed particles.[22] The shear stress distributions in the near-bed flow zone for both rigid- and mobile-bed flows are illustrated in Fig. 3(b). For the flow over a rigid bed of uniform roughness, the shear stress attains its peak value T_R^* at the reference level R^* and, then, it reduces linearly with the distance along vertical [shown by the dotted line in Fig. 3(b)]. Now, in the classical experiment of bedload transport, the transport is allowed by feeding particles from the far upstream with a rate that balances the capacity of flow to transport particles. The shear stress strikingly drops down within the saltation layer [shown by the solid line in Fig. 3(b)], which acts as an interface to separate the suspended load in the upper layer from the bedload transport in the lower layer. This reduction in shear stress arises due to the transfer of energy from the time-averaged flow to the particles in order to sustain the particle transport. Bagnold[28] reported that when a certain layer of particles is removed, the particles in the underlying layer experience a dispersive pressure as a stabilizing resistance. Therefore, the removal of particles layer by layer is caused by the interfacial fluid shear stress until it is equal to the threshold bed shear stress T_c^* [Fig. 3(b)]. Note that the finer particles are essentially transported in the suspension layer, where the flow dynamics is considered to be marginally affected by the presence of particles.

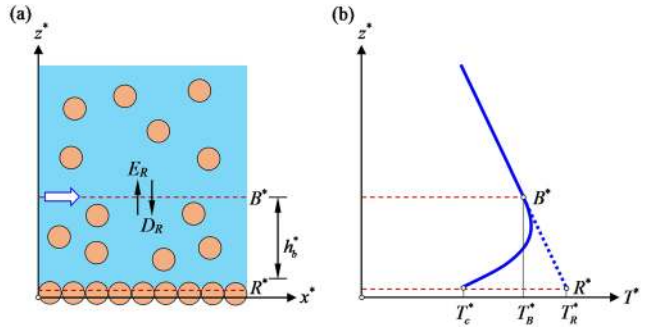

FIG. 3. Conceptual sketch of the particle transport model in the near-bed flow zone: (a) bedload and suspended load transport and (b) shear stress distribution. In (a), E_R is the entrainment rate and D_R is the deposition rate. In (b), the dotted line represents the traditional shear stress distribution for a zero-pressure gradient flow, while the solid line denotes the actual shear stress distribution in the presence of particles. Note that the shear stress is dampened within the saltation layer, which has a thickness h_b^*. Here, T_R^* and T_B^* are the shear stresses at levels R^* and B^*, respectively, whereas T_c^* is the threshold bed shear stress.

Within the saltation layer, particles are transported in a series of brief leaps. As evidenced by the measurements and also pointed out by Colombini,[11] the shear stress that drives the instability mechanism is estimated at the surface B^*. Consequently, in order to formulate the bedload flux, the T_B^* rather than T_R^* should be used, where T_B^* refers to the shear stress at level B^*. To implement the idea, we express

$$T_B = T_R(1 - B + R). \tag{18}$$

The saltation height, denoted by h_b^*, represents the distance from the summit of bed particles to the edge of the saltation layer [Fig. 3(a)]. Furthermore, the distance between the reference level R^* and the datum $z^* = 0$ is set equal to $k_s^*/30$, where the bed roughness height k_s^* scales with the particle size d^* as $k_s^* = 2.5d^*$.[29] Therefore, we set

$$B - R = h_b + \frac{d_r}{6}. \tag{19}$$

Experimental observations[30] have evidenced that the saltation height h_b^* spans up to a few particle sizes depending on the magnitude of the bed shear stress vector $\boldsymbol{T}_b^*$ in the dimensionless form, called the Shields number. It is

$$\Theta_R = \frac{|\boldsymbol{T}_b^*|}{\rho_f(s-1)gd^*}, \tag{20}$$

where s is the relative density ($= \rho_p/\rho_f$), ρ_p is the mass density of particles, and subscript "R" denotes the Shields number corresponding to the bed shear stress at the reference level R^*.

In the present formulation, we consider two important features of particle saltation, namely, the saltation height h_b^* and the mean particle velocity, V_p^*. Ali and Dey[31] compiled a large amount of experimental data of dimensionless saltation height h_b^*/d^* and mean particle velocity $V_p^*/[(s-1)gd^*]^{1/2}$ as a function of dimensionless excess bed shear stress $(\Theta_R/\Theta_c) - 1$, where Θ_c is the threshold Shields number. The experimental data[31] of h_b^*/d^* vs $(\Theta_R/\Theta_c) - 1$ and $V_p^*/[(s-1)gd^*]^{1/2}$ vs $(\Theta_R/\Theta_c) - 1$ are plotted in Figs. 4(a) and 4(b), respectively. From the experimental data trend, h_b^* and V_p^* are considered to follow the power-law relationships as

$$\frac{h_b^*}{d^*}(\Theta_R > \Theta_c) = A_h\left(\frac{\Theta_R}{\Theta_c} - 1\right)^{E_h} \text{ and } \frac{V_p^*}{[(s-1)gd^*]^{1/2}}(\Theta_R > \Theta_c) = A_v\left(\frac{\Theta_R}{\Theta_c} - 1\right)^{E_v}, \tag{21}$$

where the coefficients A_h and A_v, and the exponents E_h and E_v are set equal to 0.66, 1.61, 0.27, and 0.44, respectively. It is worth noting that the prescribed values of A_h, A_v, E_h, and E_v can be considered to be of general validity as they comply with ample experimental data compiled by Ali and Dey.[31]

Published under license by AIP Publishing

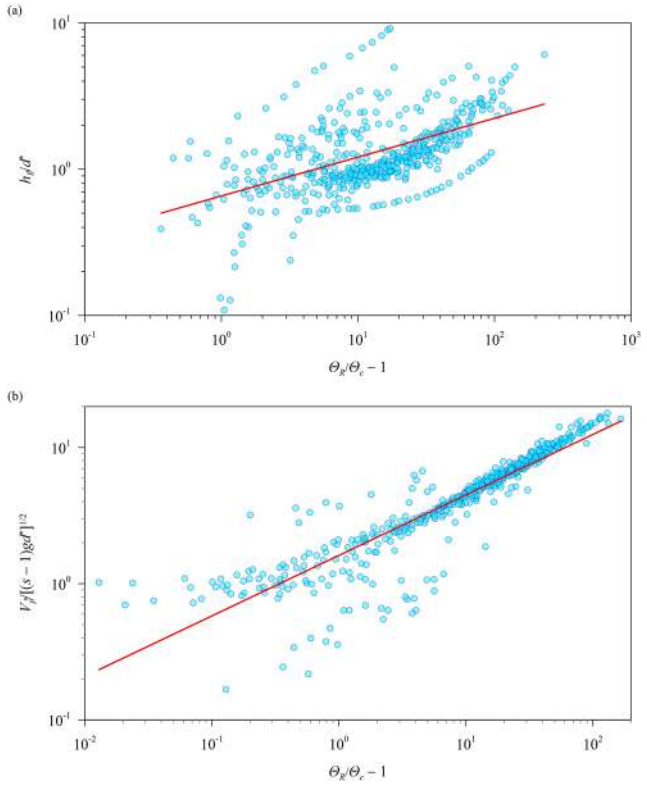

FIG. 4. (a) Dimensionless saltation height h_b^*/d^* vs dimensionless excess bed shear stress $\Theta_R/\Theta_c - 1$ and (b) mean particle velocity $V_p^*/[(s-1)gd^*]^{1/2}$ vs dimensionless excess bed shear stress $\Theta_R/\Theta_c - 1$. Solid lines represent the power-law relationships given by Eq. (21).

In Eq. (21), the Θ_c varies considerably from hydraulically smooth to rough flow regimes. Detailed analyses of the estimation of Θ_c can be found in the recent analytical studies[32–34] and state-of-the-art reviews.[35,36] However, to formulate a suitable expression for Θ_c without involving intricate analytical treatment, the viscous length scale d_v^* $[=(s-1)^{-1/3}\nu^{2/3}g^{-1}]$ is introduced. Thereafter, with the Galileo number Ga, defined as

$$Ga = \left(\frac{d^*}{d_v^*}\right)^3 = \frac{(s-1)gd^{*3}}{\nu^2}, \tag{22}$$

a complete set of conditional relationships for Θ_c can be expressed as follows:[37,38]

$$\begin{gathered}\Theta_c(0 < Ga < 43.7) = 0.141Ga^{-0.115},\\ \Theta_c(43.7 < Ga < 79\,998.5) = 0.324Ga^{-0.34}(1 + 2.04 \times 10^{-5}Ga^{1.42})^{0.35},\\ \Theta_c(Ga > 79\,998.5) = 0.045.\end{gathered} \tag{23}$$

A critical statistical analysis, performed by Dey and Ali,[36] of the experimental data of threshold of particle motion has evidenced that Eq. (23) among many others provides the best prediction for Θ_c. Furthermore, with Θ_R and Ga, the flow Froude number Fr and the roughness Reynolds number Re_k can be expressed as

$$Fr = \left[\frac{\Theta_R(s-1)d_r}{C_{f0}}\right]^{1/2} \text{ and } Re_k = Ga^{1/2}\Theta_R^{1/2}\frac{k_s}{d_r}. \tag{24}$$

When the mean particle flux is uniform, rates of erosion and deposition balance each other, suggesting that the granular bed experiences a dynamic equilibrium in the form of neither degradation nor aggradation. The bed deformation is obtained from the Exner equation. In the presence of suspended particles, the classical Exner equation is modified to take care of the effects of suspended load.[39] Let $\phi(z)$ be the local concentration of suspended particles within the suspension layer. We further define C as the depth-averaged concentration of suspended particles over the entire suspension layer with a thickness of $R + D - B$. The suspended load flux can be readily obtained from the integration of the product of the concentration of suspended particles and the velocity vector over the suspension layer thickness.[22] Under such a circumstance, the particle mass conservation equation can be approximated as

$$\begin{aligned}(1-\rho_0)\frac{\partial B}{\partial t} = &-\frac{\partial}{\partial t}[C(R+D-B)] - \left(\frac{\partial \Phi_{bx}}{\partial x} + \frac{\partial \Phi_{by}}{\partial y}\right)\\ &- \frac{Fr}{(s-1)^{1/2}d^{3/2}}\left\{\frac{\partial}{\partial x}[CU(R+D-B)]\right.\\ &\left.+ \frac{\partial}{\partial y}[CV(R+D-B)]\right\},\end{aligned} \tag{25}$$

where ρ_0 is the porosity of particles (volume of voids per unit total volume) and $\boldsymbol{\Phi}_b$ is the dimensionless bedload flux vector expressed as

$$\boldsymbol{\Phi}_b = \frac{\mathbf{Q}_b^*}{[(s-1)gd^{*3}]^{1/2}}. \tag{26}$$

In Eq. (26), $\mathbf{Q}_b^*$ is the bedload flux vector (expressed in volume per unit time and width). The time t^* is made dimensionless by introducing a parameter Q_R that accounts for the characteristic scale of the particle flux relative to that of the fluid flux as

$$t = t^*\frac{U_0^*}{D_0^*}Q_R, \text{ with } Q_R = \frac{[(s-1)gd^{*3}]^{1/2}}{U_0^*D_0^*}. \tag{27}$$

It is worth noting that the first term on the right-hand side of Eq. (25) vanishes in the present formulation because in the framework of quasi-zero-pressure gradient steady flow, the saltation layer thickness $B - R$ remains invariant with time as the bed evolves.

The effects of local streamwise and spanwise slopes on the bedload flux are modeled by considering the effective shear stress vector $\boldsymbol{T}_{eb}$ that drives the particle motion. The $\boldsymbol{T}_{eb}$ can be expressed as[40]

$$\boldsymbol{T}_{eb} = \left(T_{bx} - |\boldsymbol{T}_b|\beta\frac{\partial R}{\partial x}, T_{by} - |\boldsymbol{T}_b|\beta\frac{\partial R}{\partial y}\right). \tag{28}$$

The bedload flux vector $\boldsymbol{\Phi}_b$ is considered to align parallel to the effective bed shear stress vector $\boldsymbol{T}_{eb}$. Recalling that the local velocity vector $\boldsymbol{U}$ is also parallel to the local bed shear stress vector $\boldsymbol{T}_b$, it follows that

$$\boldsymbol{\Phi}_b = (\Phi_{bx}, \Phi_{by}) = \Phi_b\left(\cos\chi - \beta\frac{\partial R}{\partial x}, \sin\chi - \beta\frac{\partial R}{\partial y}\right), \tag{29}$$

Published under license by AIP Publishing

where

$$\cos\chi = \frac{U}{(U^2+V^2)^{1/2}} \text{ and } \beta = \beta_0\left(\frac{\Theta_c}{\Theta_B}\right)^{\beta_1}. \tag{30}$$

In Eq. (30), χ is the angle that the near-bed velocity vector makes with the streamwise direction, β is the slope factor, β_0 and β_1 are the phenomenological parameters,[40] and Θ_B is the Shields number to be evaluated at the level B^*. The β_0 can also be thought of as the ratio of threshold particle mobility for the initiation of particle motion to that of the cessation of bedload transport. In essence, $\beta_0 > 1$. Specifically, $\beta_0 = 0$ refers to vanishing effects of the local slope and $\beta_0 = \infty$ signifies an infinitely large effect of the local slope. Herein, the β_0 is considered to be reciprocal of the coefficient of dynamic friction μ_d.[41] The mean value of μ_d can be approximated as $\mu_d \approx \tan\pi/6$.[22] In addition, the β_1 is set equal to 0.5.[42] To close the physical system, it requires an appropriate relationship between the bedload flux Φ_b and the Shields number Θ. After the work of Meyer-Peter and Müller,[43] the Φ_b is considered to follow a "3/2" power-law with an excess bed shear stress, $\Theta_B - \Theta_c$, as

$$\Phi_b(\Theta_B > \Theta_c) = A_b(\Theta_B - \Theta_c)^{3/2}, \tag{31}$$

where the constant A_b is taken as 3.97 after the work of Wong and Parker.[44]

Furthermore, to obtain the transport equation of suspended particles, we consider the depth-averaged version of the advection–diffusion equation within the suspension layer.[19] Under a steady-state condition, the advection–diffusion equation can be approximated as

$$\begin{aligned}&\frac{\partial}{\partial x}[CU(R+D-B)] + \frac{\partial}{\partial y}[CV(R+D-B)]\\ &= \frac{\partial}{\partial x}\left[\frac{\nu_T}{S_N}(R+D-B)\frac{\partial C}{\partial x}\right] + \frac{\partial}{\partial y}\left[\frac{\nu_T}{S_N}(R+D-B)\frac{\partial C}{\partial y}\right]\\ &+ E_R - D_R,\end{aligned} \tag{32}$$

where E_R is the entrainment rate and D_R is the deposition rate. The difference $E_R - D_R$, being representative of the net exchange of particles through the interface between the saltation layer and the suspension layer [see Fig. 3(a)], vanishes under the equilibrium condition as considered herein. To obtain the depth-averaged concentration of suspended particles, the local concentration distribution $\phi(z)$ is integrated within the suspension layer. For $\phi(z)$, the classical Rousean formulation is revised by considering the depth-averaged form of the classical parabolic distribution for the eddy viscosity. The concentration ϕ of suspended particles scaled by its reference value C_a at the edge of the saltation layer reads[45]

$$\frac{\phi}{C_a} = \exp[-6Z(z-B)] \text{ with } Z = \frac{S_N w_s}{\kappa u_f}, \tag{33}$$

where Z is the Rouse number that qualitatively measures the settling velocity w_s^* of suspended particles relative to the friction velocity u_f^* and S_N is the turbulent Schmidt number ($\approx$1). One of the major drawbacks of the Rouse equation of the concentration of suspended particles is that it produces a vanishing concentration at the free surface.[22] By contrast, Eq. (33) predicts a finite concentration of suspended particles at the free surface. This observation is more likely for natural rivers that carry finer particle fractions. Furthermore, Eq. (33) offers a practical estimation of concentration of suspended particles in a wide open-channel flow.[22] With the above form of ϕ, the depth-averaged concentration C turns out to be

$$C = C_a\frac{1-\exp\left[-6Z\left(1-\frac{d_r}{6}-h_{b0}\right)\right]}{6Z\left(1-\frac{d_r}{6}-h_{b0}\right)}. \tag{34}$$

In Eq. (34), the reference concentration C_a at the edge of the saltation layer can be found from the relationship $\left|\mathbf{Q}_b^*\right| = C_a h_b^* V_p^*$.[22] Using Eqs. (21) and (26), the C_a takes the form of

$$C_a = \frac{\Phi_b}{A_h A_v}\left(\frac{\Theta_R}{\Theta_c}-1\right)^{-(E_h+E_v)}. \tag{35}$$

Furthermore, as the settling velocity w_s^* depends on particle size d^*, the three key numbers, such as the Rouse number Z, Shields number Θ, and Galileo number Ga, can be linked together. To this end, we recall the empirical relationship of Jiménez and Madsen.[46] For natural sediment particles, it is expressed as

$$f(Ga) = \frac{w_s^*}{[(s-1)gd^*]^{1/2}} = \left(0.954 + \frac{20.48}{Ga^{1/2}}\right)^{-1}. \tag{36}$$

The above formulation was developed for the particle size range 0.063 mm–1 mm. However, it has been found that Eq. (36) produces comparable predictions (with respect to other formulas) of the settling velocity over the entire sand range (0.063 mm $< d^* <$ 2 mm). Note that Eq. (36) was found to yield the best result for fine sand with the nominal size range of 0.063 mm–0.25 mm, for which the particles are likely to be transported as a suspended load.[46] With the above functional form, the Rouse number Z can be expressed as

$$Z = f(Ga)\frac{S_N}{\kappa\Theta^{1/2}}. \tag{37}$$

IV. LINEARIZATION

Following the standard linearization procedure, the physical system is solved in terms of normal modes. In the linearization, a generic quantity can be expressed as

$$P(x,y,t) = P_0 + \delta P_1(x,y,t), \tag{38}$$

$$P_1(x,y,t) = AP_{11}L(x,y,t) + \text{c.c.}$$

with

$$L = \exp[\mathrm{i}(n_x x - \Omega t)]\exp(\mathrm{i}n_y y), \tag{39}$$

where δ is a small parameter, A is an arbitrary factor, c.c. stands for complex conjugate, $\boldsymbol{n}$ is the dimensionless wave vector, and Ω is the complex wave celerity. Note that with regard to the formation of large-scale riverbed patterns (e.g., river bars), the dimensionless streamwise and spanwise wavenumbers, denoted by n_x and n_y, respectively, can be expressed as

$$n_x = \frac{2\pi D^*}{l_x^*} \text{ and } n_y = \frac{2\pi D^*}{l_y^*} = \frac{\pi}{2\vartheta}, \tag{40}$$

where l_x^* and l_y^* are the streamwise and spanwise wavelengths, respectively. In the above equation, the l_y^* can be taken to be twice the channel width ($= 4W^*$, where W^* is the channel halfwidth) so

Published under license by AIP Publishing

that ϑ defines the channel aspect ratio (ratio of channel halfwidth to flow depth).

Using Eqs. (38) and (39), the conductance coefficient and the eddy viscosity can be expanded as

$$C_f = C_{f0}\{1 + [(s_1 - 2)U_{11} + s_2 D_{11}]AL\delta\} + O(\delta^2), \tag{41}$$

$$\nu_T = \nu_{T0}[1 + (s_3 K_{11} + s_4 \varepsilon_{11})AL\delta] + O(\delta^2), \tag{42}$$

where s_i is a set of coefficients. The undisturbed dissipation rate of TKE can be estimated from Eq. (6) using the conventional formulation for the undisturbed eddy viscosity as $\nu_{T0} = \kappa u_{f0}/6$ and the expression for the undisturbed TKE from Eq. (17).

Using the above relationships, the continuity and momentum equations [see Eqs. (2)–(4)] at the leading order $O(\delta)$ produce the following algebraic equations:

$$n_x U_{11} + n_y V_{11} + n_x D_{11} = 0, \tag{43}$$

$$\begin{aligned}&(\mathrm{i}n_x + 2\nu_{T0} n_x^2 + \nu_{T0} n_y^2 + s_1 C_{f0}) U_{11} + \nu_{T0} n_x n_y V_{11} \\ &\quad + \left[\mathrm{i}n_x\left(\frac{1}{Fr^2} + \frac{2K_0}{3}\right) + (s_2 - 1)C_{f0}\right] D_{11} + \frac{\mathrm{i}n_x}{Fr^2} R_{11} + \frac{2}{3}\mathrm{i}n_x K_{11} = 0,\end{aligned} \tag{44}$$

$$\begin{aligned}&\nu_{T0} n_x n_y U_{11} + (\mathrm{i}n_x + \nu_{T0} n_x^2 + 2\nu_{T0} n_y^2 + C_{f0}) V_{11} + \mathrm{i}n_y\left(\frac{1}{Fr^2} + \frac{2K_0}{3}\right) D_{11} \\ &\quad + \frac{\mathrm{i}n_y}{Fr^2} R_{11} + \frac{2}{3}\mathrm{i}n_y K_{11} = 0.\end{aligned} \tag{45}$$

Applying the linearization procedure, it has been found that the production rate term P_H has no contribution to the linear stability analysis, while the terms P_{KV} and $P_{\varepsilon V}$ are expanded as follows:

$$P_{KV} = C_{f0}\{1 + [(s_1 + 1)U_{11} + (s_2 - 1)D_{11}]AL\delta\} + O(\delta^2), \tag{46}$$

$$P_{\varepsilon V} = s_5\left\{1 + \left[\left(\frac{5}{4}s_1 + \frac{3}{2}\right)U_{11} + \left(\frac{5}{4}s_2 - 2\right)D_{11}\right]AL\delta\right\} + O(\delta^2). \tag{47}$$

Furthermore, the linearized transport equations of the TKE and its dissipation rate [see Eqs. (7) and (8)] are obtained as

$$\begin{aligned}&(s_1 + 1)C_{f0}U_{11} + (s_2 - 1)C_{f0}D_{11} \\ &\quad - \left(\mathrm{i}n_x + \frac{\nu_{T0}}{\sigma_K} n_x^2 + \frac{\nu_{T0}}{\sigma_K} n_y^2\right) K_{11} - \varepsilon_{11} = 0,\end{aligned} \tag{48}$$

$$\begin{aligned}&s_5\left(\frac{5}{4}s_1 + \frac{3}{2}\right)U_{11} + s_5\left(\frac{5}{4}s_2 - 2\right)D_{11} + c_{2\varepsilon}\left(\frac{\varepsilon_0}{K_0}\right)^2 K_{11} \\ &\quad - \left(\mathrm{i}n_x + \frac{\nu_{T0}}{\sigma_\varepsilon} n_x^2 + \frac{\nu_{T0}}{\sigma_\varepsilon} n_y^2 + 2c_{2\varepsilon}\frac{\varepsilon_0}{K_0}\right)\varepsilon_{11} = 0.\end{aligned} \tag{49}$$

Moreover, in the present formulation, the saltation height is considered to be a perturbed quantity so that the h_b takes the form of

$$h_b = h_{b0}[1 + s_6(s_1 U_{11} + s_2 D_{11})AL\delta] + O(\delta^2). \tag{50}$$

The intensity of bedload flux can be expanded as

$$\Phi_b = \Phi_{b0}[1 + (s_7 U_{11} + s_8 D_{11})AL\delta] + O(\delta^2). \tag{51}$$

Therefore, the equations related to the bed evolution [see Eqs. (19), (25), and (32)] at the leading order $O(\delta)$ yield

$$h_{b0} s_1 s_6 U_{11} + h_{b0} s_2 s_6 D_{11} + R_{11} - B_{11} = 0, \tag{52}$$

$$\begin{aligned}&-(1 - \rho_0)\mathrm{i}\Omega B_{11} + \Phi_{b0}\beta(n_x^2 + n_y^2)R_{11} \\ &+ \mathrm{i}n_x\left[s_7\Phi_{b0} - s_1 s_6 s_9 h_{b0} C_0 + s_9\left(1 - \frac{d_r}{6} - h_{b0}\right)C_0\right]U_{11} \\ &+ \mathrm{i}n_y\left[\Phi_{b0} + s_9\left(1 - \frac{d_r}{6} - h_{b0}\right)C_0\right]V_{11} \\ &\mathrm{i}n_x[s_8\Phi_{b0} + s_9(1 - s_2 s_6 h_{b0})C_0]D_{11} + \mathrm{i}n_x s_9\left(1 - \frac{d_r}{6} - h_{b0}\right)C_{11} = 0,\end{aligned} \tag{53}$$

$$\begin{aligned}&\mathrm{i}n_x\left(1 - \frac{d_r}{6} - h_{b0} - s_1 s_6 h_{b0}\right)C_0 U_{11} + \mathrm{i}n_y\left(1 - \frac{d_r}{6} - h_{b0}\right)C_0 V_{11} \\ &\quad + \mathrm{i}n_x(1 - s_2 s_6 h_{b0})C_0 D_{11} + \left(1 - \frac{d_r}{6} - h_{b0}\right) \\ &\quad \times\left[\mathrm{i}n_x + \frac{\nu_{T0}}{S_N}(n_x^2 + n_y^2)\right]C_{11} = 0.\end{aligned} \tag{54}$$

It is worth mentioning that in the above linearized equations, the complete set of coefficients s_i with $i = 1$–9 is expressed as

$$\begin{aligned}&s_1 = 2\left(1 - \frac{\Theta_0}{C_{f0}}\frac{\partial C_f}{\partial\Theta}\right)^{-1},\ s_2 = \frac{1}{C_{f0}}\frac{\partial C_f}{\partial D}\left(1 - \frac{\Theta_0}{C_{f0}}\frac{\partial C_f}{\partial\Theta}\right)^{-1}, \\ &s_3 = \frac{2}{K_0},\ s_4 = -\frac{1}{\varepsilon_0},\ s_5 = \frac{c_{2\varepsilon} c_\mu^{1/2} C_{f0}^{5/4}}{a_0^{1/2}}, s_6 = \frac{\Theta_0}{h_{b0}}\frac{\partial h_b}{\partial\Theta}, \\ &s_7 = \frac{\Theta_0}{\Phi_{b0}}\frac{\partial\Phi_b}{\partial\Theta}s_1,\ s_8 = \frac{\Theta_0}{\Phi_{b0}}\frac{\partial\Phi_b}{\partial\Theta}s_2, \text{ and } s_9 = \frac{Fr}{(s-1)^{1/2} d_r^{3/2}}.\end{aligned} \tag{55}$$

In Eq. (55), all the derivatives have been evaluated at the undisturbed state. The set of equations accompanying eight variables $\boldsymbol{X} = (U_{11}, V_{11}, D_{11}, R_{11}, B_{11}, K_{11}, \varepsilon_{11}, C_{11})^T$ can be expressed in the matrix form of $\boldsymbol{CX} = 0$, where $\boldsymbol{C}$ is the coefficient matrix. The elimination of variables from the set of equations provides a direct estimation of the complex growth rate of the system. The resulting expression being complicated would take substantial space and therefore is not furnished herein. However, this reflects a direct balance between the stabilizing effects due to the gravity and the destabilizing effects due to the particle transport aided by the bed shear stress. Furthermore, the role of the depth-averaged turbulence-state is subtler, since it is closely tied-up with the local bed shear stress vector.

With the above formulation, the growth rate of bed perturbation Ω^G can be readily obtained as a function of streamwise and spanwise wavenumbers, n_x and n_y, and of three key entities, namely, the Galileo number Ga, Shields number Θ, and relative roughness d_r. The introduction of the Galileo number essentially reflects the role of flow regime in accordance with Eq. (24) and that of the Rouse number given by Eq. (37). The other two entities, Θ and d_r, shed light on the effects of the flow Froude number and friction factor, respectively. The Ω^G is expressed as

$$\Omega^G = \mathrm{Im}(\Omega)C_f^{1/2}. \tag{56}$$

Published under license by AIP Publishing

V. RESULTS AND DISCUSSION

To discuss the results obtained from the linear theory, we perform four numerical experiments (Figs. 5–8). In these experiments, we aim at exploring how the large-scale riverbed patterns evolve on the wavenumber plane when the key parameters related to the flow and particles vary over a wide range.

The first numerical experiment highlights the emergence of instability in smooth and transitional flow regimes, as the Θ_R/Θ_c ratio increases (Fig. 5). To track smooth and transitional flow regimes, the Galileo number is kept constant as $Ga = 25$. In a subaqueous environment, this value of Ga corresponds to the particle size of 0.115 mm, which typically represents the finer sand size. Note that the Θ_R/Θ_c ratio increases in each panel of Fig. 5, suggesting that the roughness Reynolds number also increases in the corresponding panel. Moreover, in each panel, the relative roughness is set equal to $d_r = 0.005$. It turns out that the dimensional flow depth is the same in all the panels of Fig. 5. Since in each panel, the flow depth is kept constant, the variations in the spanwise wavenumber, being scaled with the depth to width ratio [see Eq. (40)], correspond to a change in the channel width.

The stability maps for the first experiment are highlighted in Fig. 5 on a logarithmic scale. The solid line indicates the marginal stability curves, given by $\Omega^G = 0$, and embraces the instability region ($\Omega^G > 0$). Figure 5 clearly depicts the evolutions of bar instability, as the Θ_R/Θ_c ratio increases. For a small Θ_R/Θ_c ratio [Fig. 5(a)], the instability region appears to be similar to that of alternate patterns of river bars.[15] The instability region is approximately bounded by $n_x \in (10^{-2}, 8 \times 10^{-1})$ and $n_y \in (10^{-2}, 10^{-1})$, and the maximum amplification of the pattern corresponds to $(n_x, n_y) \approx (10^{-1}, 1.2 \times 10^{-1})$. The marginal stability curve indicates that beyond a threshold spanwise wavenumber n_{yc}, patterns are stable. This also suggests that the channel aspect ratio must exceed its threshold value for the formation of large-scale patterns, an observation being in agreement with the classical theories of bar instability and the experimental observations.[15] As the flow strength increases [Figs. 5(b) and 5(c)], the bar pattern tends to stretch with an additional lower marginal stability curve close to shorter streamwise and spanwise wavenumbers. The maximum amplification of patterns also enhances toward longer wavenumbers, destabilizing the patterns for lower channel aspect ratios. The growth rate of bed perturbation appears to increase with the increase in the Θ_R/Θ_c ratio.

Note that for a given Galileo number (or particle size), the dimensional settling velocity obtained from Eq. (36) remains a constant. As the Rouse number reflects the ratio of the settling velocity to shear velocity [see Eq. (33)], with an increase in the Θ_R/Θ_c ratio in each panel, it refers to a decrease in the Rouse number, resulting in significant effects of particle suspension. Therefore, in the so-called upper flow regime (flow Froude number >1), the instability patterns change strikingly. Therefore, as the flow strength increases further, the destabilizing effects become more encouraging, with a shift of the maximum amplification of patterns toward longer wavenumbers [Figs. 5(d)–5(f)]. However, the patterns having shorter wavenumbers become stable as the Θ_R/Θ_c ratio increases because the lower marginal stability curve tends to grow with an increase in the Θ_R/Θ_c ratio [Figs. 5(a)–5(f)]. This is attributed to the subtle effects of sediment suspension, destabilizing longer wavenumbers and stabilizing shorter wavenumbers.

The second numerical experiment examines the stability maps in a rough flow regime, as the Θ_R/Θ_c ratio increases (Fig. 6). In the experiment, the typical value of the Galileo number is taken as $Ga = 2.25 \times 10^4$, which corresponds to the particle size of 1.116 mm,

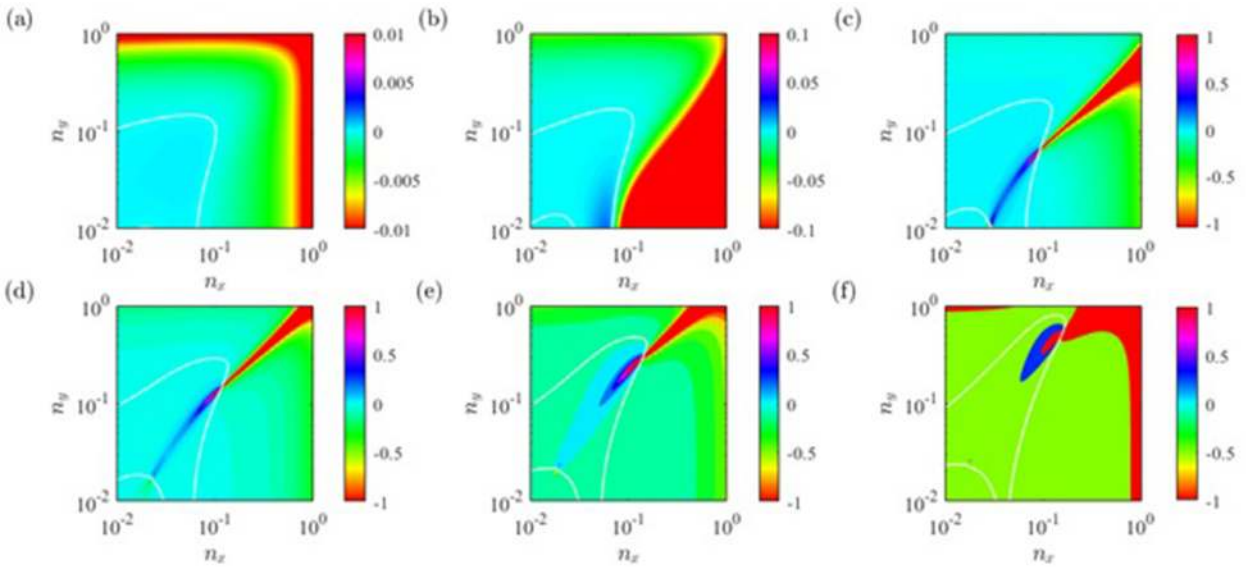

FIG. 5. Effects of the Shields number on the stability maps in smooth and transitional flow regimes ($Ga = 25$) for $d_r = 0.005$: (a) $\Theta_R/\Theta_c = 2$, (b) $\Theta_R/\Theta_c = 4$, (c) $\Theta_R/\Theta_c = 6$, (d) $\Theta_R/\Theta_c = 10$, (e) $\Theta_R/\Theta_c = 20$, and (f) $\Theta_R/\Theta_c = 40$. Color bars refer to the growth rate of bed perturbation Ω^G, and solid lines (white) signify the marginal stability curves ($\Omega^G = 0$).

Published under license by AIP Publishing

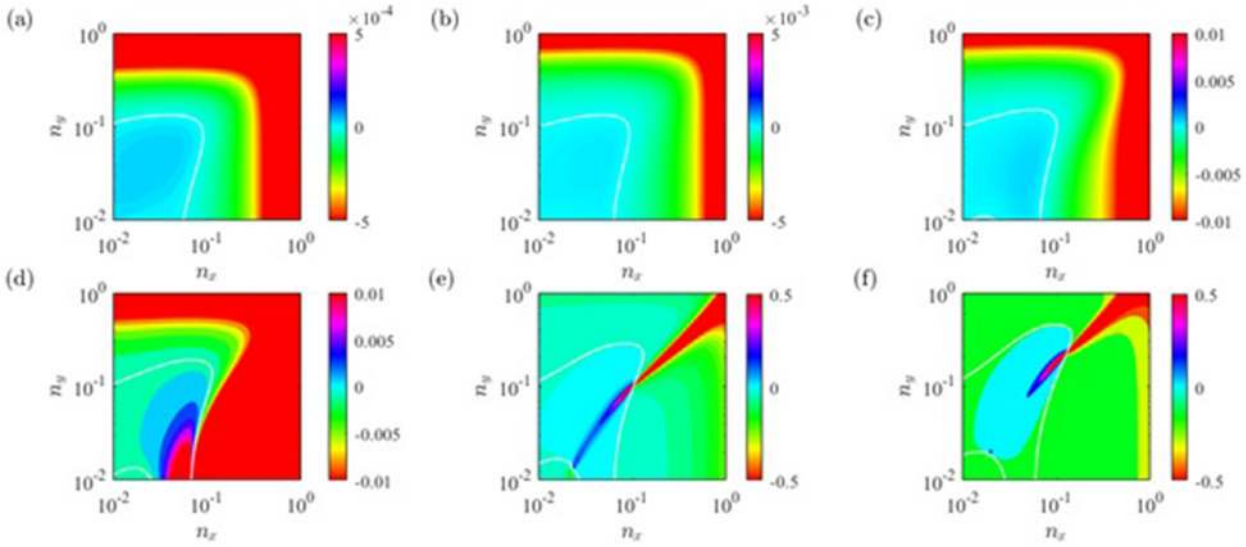

FIG. 6. Effects of the Shields number on the stability maps for a rough flow regime ($Ga = 2.25 \times 10^4$) for $d_r = 0.005$: (a) $\Theta_R/\Theta_c = 2$, (b) $\Theta_R/\Theta_c = 4$, (c) $\Theta_R/\Theta_c = 6$, (d) $\Theta_R/\Theta_c = 10$, (e) $\Theta_R/\Theta_c = 20$, and (f) $\Theta_R/\Theta_c = 40$.

being representative of the very coarse sand size. In addition, the relative roughness is set equal to 0.005, as considered in Fig. 5. With respect to the small Θ_R/Θ_c ratio in smooth and transitional flow regimes [Fig. 5(a)], the stability map in Fig. 6(a) reveals that the instability region of bars slightly reduces. The qualitative variations of bar instability with the Θ_R/Θ_c ratio in Figs. 6(a)–6(f) appear to be similar to those illustrated in smooth and transitional flow regimes [see Figs. 5(a)–5(f)]. However, for a given Θ_R/Θ_c ratio, the bar pattern appears to be slightly more stable in a rough flow regime. The reason is ascribed to the fact that for a given Θ_R/Θ_c ratio in the bar mode, the maximum amplification of patterns lessens in a rough flow regime [for instance, compare Figs. 5(c) and 6(c)]. In consequence, the instability region is reduced. Furthermore, for a given Θ_R/Θ_c ratio, the growth rate of bed perturbation in a rough flow regime reduces compared to those in smooth and transitional flow regimes. Moreover, the appearance of the lower marginal stability curve in a rough flow regime is delayed when compared to those in smooth and transitional flow regimes. For instance, in smooth and transitional flow regimes, the lower marginal stability curve is evident for $\Theta_R/\Theta_c = 4$ [Fig. 5(b)], whereas in a rough flow regime, it does not appear for $\Theta_R/\Theta_c = 4$ [Fig. 6(b)]. In fact, it is noticeable once the Θ_R/Θ_c ratio exceeds 6 [Figs. 6(d)–6(f)].

In this context, we remark that the classical theories[15,17,18] have not been able to draw the above conclusions because most of the existing theories on the instability of large-scale riverbed patterns are not capable of addressing simultaneously both the crucial effects of flow regimes and particle suspension.

Note that in Figs. 5 and 6, the stability maps are analyzed for a given relative roughness ($d_r = 0.005$). However, a change in relative roughness corresponds to a change in the friction factor, in accordance with Eq. (12). Therefore, it is interesting to analyze the behavior of stability maps in smooth, transitional, and rough flow regimes when the relative roughness changes over a certain range. To this end, we perform another two numerical experiments as furnished below.

The third numerical experiment aims at exploring the stability maps in smooth and transitional flow regimes ($Ga = 25$) as the relative roughness d_r increases (Fig. 7). The Θ_R/Θ_c ratio is taken as $\Theta_R/\Theta_c = 5$. Since the particle size is kept as a constant (because Ga is kept as a constant), with an increase in relative roughness, it refers to a decrease in flow depth. The effects of relative roughness on the stability maps are tested for six different values of d_r corresponding to a given Θ_R/Θ_c ratio [Figs. 7(a)–7(f)]. For a small relative roughness [Fig. 7(a)], the instability region is bounded by the upper and lower marginal stability curves. However, as the relative roughness increases, the instability region appears to contract [Figs. 7(b) and 7(c)]. The contraction is more apparent in the lower limb of the marginal curve for $n_x \in (3 \times 10^{-2}, 6 \times 10^{-2})$. The instability region appears to be tapered, as the maximum amplification of the pattern has a tendency to shift toward longer wavenumbers [Fig. 7(c)]. The growth rate of bed perturbation reduces as the relative roughness increases. As the relative roughness increases further [Figs. 7(d)–7(f)], the instability region becomes more tapered, and the patterns with shorter streamwise wavenumbers (say, $n_x \approx 10^{-2}$) become stable even for a shorter spanwise wavenumber range $n_y \in (10^{-2}, 2 \times 10^{-2})$ (large channel aspect ratios). In addition, the maximum amplification of patterns appears to shift toward longer wavenumbers [in both streamwise and spanwise directions; see Figs. 7(d)–7(f)].

The fourth numerical experiment sheds light on the stability maps in a rough flow regime ($Ga = 2.25 \times 10^4$) as the relative roughness increases (Fig. 8). In the experiment, $\Theta_R/\Theta_c = 5$ is considered as in Fig. 7. In general, the qualitative features of instability in Fig. 8 are similar to those in Fig. 7. However, for a small relative

Published under license by AIP Publishing

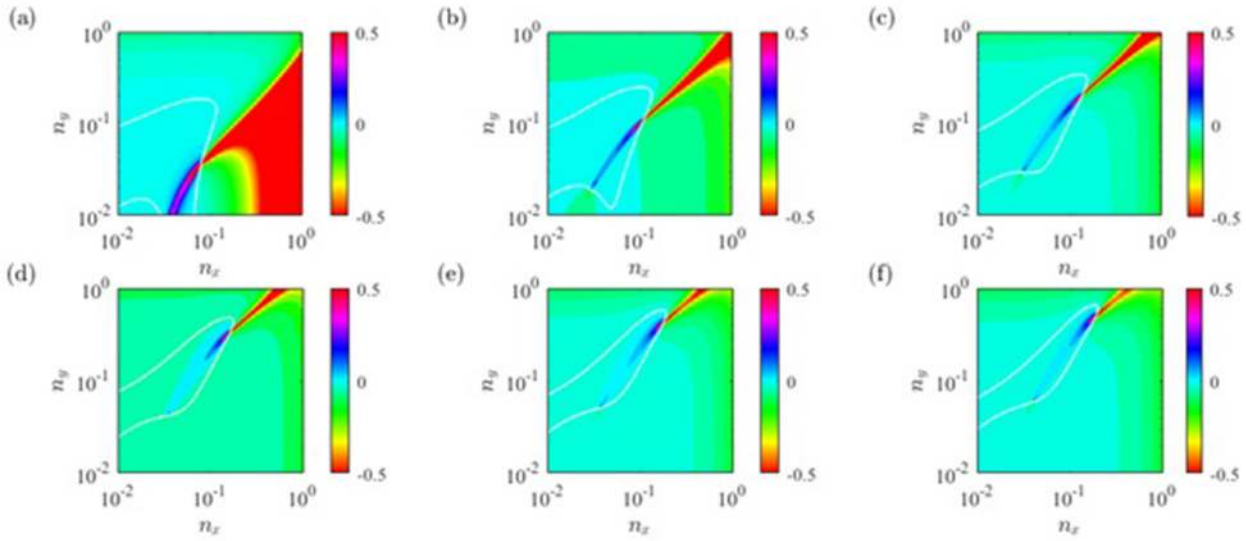

FIG. 7. Effects of relative roughness on the stability maps in smooth and transitional flow regimes (Ga = 25) for Θ_R/Θ_c = 5: (a) d_r = 0.005, (b) d_r = 0.01, (c) d_r = 0.02, (d) d_r = 0.04, (e) d_r = 0.06, and (f) d_r = 0.08.

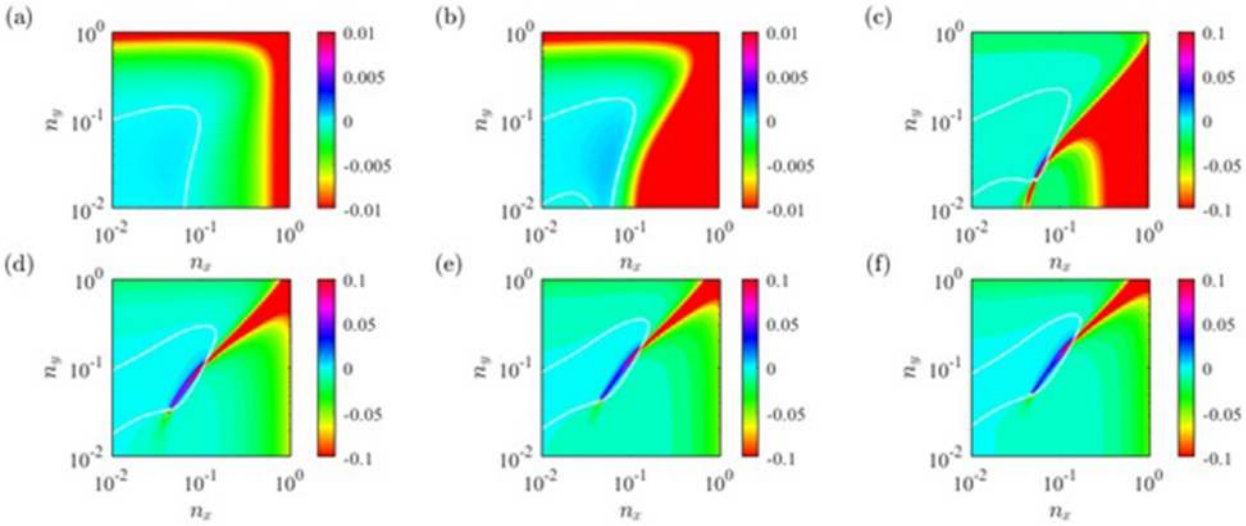

FIG. 8. Effects of relative roughness on the stability maps in a rough flow regime (Ga = 2.25 × 10^4) for Θ_R/Θ_c = 5: (a) d_r = 0.005, (b) d_r = 0.01, (c) d_r = 0.02, (d) d_r = 0.04, (e) d_r = 0.06, and (f) d_r = 0.08.

roughness, the marginal stability curves appear to be less contracted compared to those in smooth and transitional flow regimes [for instance, compare Figs. 7(b) and 8(b)]. The stability maps reveal that the magnitude of the growth rate of bed perturbation in a rough flow regime reduces compared to those in smooth and transitional flow regimes [compare Figs. 7(b) and 8(b)]. As expected, the maximum amplification of patterns shifts toward longer streamwise and spanwise wavenumbers with an increase in relative roughness [Figs. 8(d)–8(f)]. However, for a given relative roughness, the maximum amplification of patterns in a rough flow regime diminishes compared to those in smooth and transitional flow regimes [compare Figs. 7(e) and 8(e)].

In essence, this study offers insight into the instability of large-scale riverbed patterns. It is worth noting that the present analysis, keeping in mind the open questions and research gaps as delineated in the Introduction, is primarily focused on the instability of large-scale patterns from a linear approach. The linear stability analysis offers a useful tool in order to predict the stable and unstable

Published under license by AIP Publishing

patterns on the wavenumber plane over a wide practical range of river flows. The model results can provide a preliminary guideline in predicting the possible qualitative patterns in gravel-bed rivers and rivers carrying high concentration of sediment suspension. In this context, it is pertinent to mention that the nonlinear analysis may be useful to anticipate the height perturbations of large-scale patterns. In a recent attempt,[18] a weakly nonlinear model was proposed by applying the center manifold projection technique. The sediment suspension acts to destabilize the large-scale patterns. In particular, it influences both the wavenumber in a linear model and the amplitude in a nonlinear model. The present study clearly shows how the sediment suspension affects the bar instability in various flow regimes. In this regard, to gain more insight into the instability mechanism, a full nonlinear model including the effects of the flow regime and various modes of sediment transport may be developed as a future scope of research.

VI. CONCLUSIONS

In this study, the instability of large-scale riverbed patterns in a wide straight channel is investigated wherein a linear stability analysis is carried out with the aid of a suitable flow model coupled with the transport equations of the TKE and its dissipation rate and the particle transport model. In this regard, the subtle effects of flow regimes and particle suspension are taken into account. The stability maps depict the evolution of riverbed patterns, depending on the streamwise and spanwise wavenumbers, and the parameter space associated with flow and particles.

In smooth and transitional flow regimes, for a given relative roughness, the instability zone tends to stretch as the Shields number increases, with an additional marginal stability curve close to shorter wavenumbers. The maximum amplification enhances toward longer wavenumbers, and the growth rate of bed perturbation increases with an increase in the Shields number. In a rough flow regime, for a given relative roughness and Shields number, the instability region slightly reduces compared to those in smooth and transitional flow regimes. However, the bar pattern becomes slightly more stable in a rough flow regime. In a rough flow regime, the growth rate of bed perturbation diminishes and the lower marginal stability curve appears to be delayed when compared to those in smooth and transitional flow regimes. In smooth and transitional flow regimes, for a given Shields number, the instability region contracts with an increase in relative roughness. The growth rate of bed perturbation lessens and the maximum amplification of patterns shifts toward longer wavenumbers as the relative roughness increases. The growth rate of bed perturbation in a rough flow regime reduces compared to those in smooth and transitional flow regimes. The maximum amplification of patterns in a rough flow regime, for a given relative roughness, reduces compared to those in smooth and transitional flow regimes.

Although this study sheds light on the instability of three-dimensional large-scale riverbed patterns, a crucial question is yet to be addressed: how do the patterns evolve in a macro-rough-bed flow? This requires particular attention because of the complexity arising from the near-bed spatiotemporal heterogeneous flow. Under such circumstances, the classical instability theories may not be able to precisely mimic the fluid–particle interplay. To this end, a concrete numerical model may be developed as a future scope of research.

ACKNOWLEDGMENTS

S.D. acknowledges the J. C. Bose Fellowship Award [funded by DST, Science and Engineering Research Board (SERB), Grant Reference No. JCB/2018/000004] in pursuing this work.

NOMENCLATURE

Θ_B	Shields number corresponding to T_B^*
Θ_c	threshold Shields number
Θ_R	Shields number corresponding to T_R^*
β	slope factor
δ	small parameter
δ_{ij}	Kronecker delta function
ε	depth-averaged TKE dissipation rate
$\boldsymbol{\Phi}_b$	dimensionless bedload flux vector
Ω	complex wave celerity
Ω^G	growth rate of bed perturbation
κ	von Kármán coefficient
λ_b	Darcy–Weisbach friction factor
μ_d	coefficient of dynamic friction
ν_T	$\nu_T^*/(U_0^* D_0^*)$
ν_T^*	eddy viscosity
ρ_f	mass density of fluid
ρ_p	mass density of particles
ρ_0	porosity of particles
σ_i^*	ith turbulence intensity
υ	coefficient of kinematic viscosity of fluid
χ	angle between near-bed velocity vector and streamwise direction
ϑ	channel aspect ratio
ϕ	local concentration of suspended particles
a_0	$\nu_T^*/u_f^* D^*$
B	B^*/D_0^*
B^*	top edge of the saltation layer
C	depth-averaged concentration of suspended particles
C_a	reference concentration
C_f	conductance coefficient
d^*	particle size
d_r	d^*/D_0^*
d_ν^*	$(s-1)^{-1/3}\upsilon^{2/3}g^{-1}$
D	D^*/D_0^*
D^*	local flow depth
D_R	deposition rate
D_0^*	undisturbed flow depth
E_R	entrainment rate
Fr	flow Froude number
g	gravitational acceleration
Ga	Galileo number
h_b	h_b^*/D_0^*
h_b^*	saltation height
k^*	TKE
k_s	k_s^*/D_0^*
k_s^*	bed roughness height
K	depth-averaged TKE

Published under license by AIP Publishing

l_x^*	streamwise wavelength
l_y^*	spanwise wavelength
$\boldsymbol{n}$	wave vector [$=(n_x, n_y)$]
n_{yc}	threshold spanwise wavenumber
P_H	production rate of K arising from horizontal velocity gradients
$(P_{KV}, P_{\varepsilon V})$	production rates of (K, ε) arising from vertical velocity gradients
$\boldsymbol{Q}$	dispersion terms
$\boldsymbol{Q}_b^*$	bedload flux vector
Q_R	$[(s-1)gd^{*3}]^{1/2}/(U_0^* D_0^*)$
R	R^*/D_0^*
R^*	reference level
Re	flow Reynolds number
Re_k	roughness Reynolds number
s	relative density ($=\rho_p/\rho_f$)
S_N	turbulent Schmidt number
t	$t^*(U_0^*/D_0^*)Q_R$
t^*	time
$\boldsymbol{T}$	$\boldsymbol{T}^*/(\rho_f U_0^{*2})$
$\boldsymbol{T}^*$	stress tensor
$\boldsymbol{T}_b$	$\boldsymbol{T}_b^*/(\rho_f U_0^{*2})$
$\boldsymbol{T}_b^*$	bed shear stress vector
T_B	$T_B^*/(\rho_f U_0^{*2})$
T_B^*	shear stress at B^*
T_c^*	threshold bed shear stress
$\boldsymbol{T}_{eb}$	effective shear stress vector
T_{ij}	turbulent stress tensor
T_R	$T_R^*/(\rho_f U_0^{*2})$
T_R^*	shear stress at R^*
u_f	u_f^*/U_0^*
u_f^*	friction velocity
$\boldsymbol{U}$	$\boldsymbol{U}^*/U_0^*$
$\boldsymbol{U}^*$	local depth-averaged velocity vector
U_0^*	depth-averaged undisturbed streamwise velocity
V_p^*	mean particle velocity
w_s	w_s^*/U_0^*
w_s^*	settling velocity
W^*	channel halfwidth
(x, y, z)	$(x^*, y^*, z^*)/D_0^*$
x^*	streamwise distance
y^*	spanwise distance
z^*	vertical distance
Z	Rouse number

Superscript

$*$	dimensional variable

Subscript

0	undisturbed state of a variable

DATA AVAILABILITY

The data that support the findings of this study are available from the corresponding author upon reasonable request.

REFERENCES

[1] J. F. Kennedy, "The formation of sediment ripples, dunes, and antidunes," Annu. Rev. Fluid Mech. **1**, 147–168 (1969).
[2] F. Engelund and J. Fredsøe, "Sediment ripples and dunes," Annu. Rev. Fluid Mech. **14**, 13–37 (1982).
[3] J. B. Southard, "Experimental determination of bed-form stability," Annu. Rev. Earth Planet. Sci. **19**, 423–455 (1991).
[4] F. Charru, B. Andreotti, and P. Claudin, "Sand ripples and dunes," Annu. Rev. Fluid Mech. **45**, 469–493 (2013).
[5] M. Colombini, "A decade's investigation of the stability of erodible stream beds," J. Fluid Mech. **756**, 1–4 (2014).
[6] G. Seminara, "Fluvial sedimentary patterns," Annu. Rev. Fluid Mech. **42**, 43–66 (2010).
[7] S. Dey and S. Z. Ali, "Fluvial instabilities," Phys. Fluids **32**, 061301 (2020).
[8] S. K. Bose and S. Dey, "Reynolds averaged theory of turbulent shear flows over undulating beds and formation of sand waves," Phys. Rev. E **80**, 036304 (2009).
[9] S. K. Bose and S. Dey, "Instability theory of sand-ripples formed by turbulent shear flows," J. Hydraul. Eng. **138**, 752–756 (2012).
[10] K. J. Richards, "The formation of ripples and dunes on an erodible bed," J. Fluid Mech. **99**, 597–618 (1980).
[11] M. Colombini, "Revisiting the linear theory of sand dune formation," J. Fluid Mech. **502**, 1–16 (2004).
[12] M. Colombini and A. Stocchino, "Finite-amplitude river dunes," J. Fluid Mech. **611**, 283–306 (2008).
[13] M. Colombini and A. Stocchino, "Ripple and dune formation in rivers," J. Fluid Mech. **673**, 121–131 (2011).
[14] M. Colombini and A. Stocchino, "Three-dimensional river bed forms," J. Fluid Mech. **695**, 63–80 (2012).
[15] M. Colombini, G. Seminara, and M. Tubino, "Finite-amplitude alternate bars," J. Fluid Mech. **181**, 213–232 (1987).
[16] A. Crosato and E. Mosselman, "An integrated review of river bars for engineering, management and transdisciplinary research," Water **12**(2), 596 (2020).
[17] M. Tubino, R. Repetto, and G. Zolezzi, "Free bars in rivers," J. Hydraul. Res. **37**, 759–775 (2010).
[18] M. B. Bertagni and C. Camporeale, "Finite amplitude of free alternate bars with suspended load," Water Resour. Res. **54**(12), 9759–9773, https://doi.org/10.1029/2018wr022819 (2018).
[19] B. M. Duc, T. Wenka, and W. Rodi, "Numerical modeling of bed deformation in laboratory channels," J. Hydraul. Eng. **130**, 894–904 (2004).
[20] W. Rodi, *Turbulence Models and Their Applications in Hydraulics* (Balkema, Rotterdam, The Netherlands, 1993).
[21] ASCE Task Force, "Friction factor in open channels," J. Hydraul. Div. **89**, 97–143 (1963).
[22] S. Dey, *Fluvial Hydrodynamics: Hydrodynamic and Sediment Transport Phenomena* (Springer-Verlag, Berlin, Germany, 2014).
[23] I. Nezu, "Turbulent structure in open channel flow," Ph.D. thesis, Kyoto University, Kyoto, 1977.
[24] I. Nezu and H. Nakagawa, *Turbulence in Open-Channel Flows* (Balkema, Rotterdam, The Netherlands, 1993).
[25] B. A. Kironoto and W. H. Graf, "Turbulence characteristics in rough uniform open-channel flow," Water Marit. Energy **106**, 333–344 (1994).
[26] V. Nikora and D. Goring, "Spectral scaling for gravel-bed open-channel flows," in *Proceedings of the NATO Advanced Research Workshop on Stochastic Models of Hydrological Processes and their Applications to Problems of Environmental Preservation* (Water Problems Institute, Moscow, 1998), pp. 239–245.
[27] V. Nikora and D. Goring, "Flow turbulence over fixed and weakly mobile gravel beds," J. Hydraul. Eng. **126**, 679–690 (2000).
[28] R. A. Bagnold, "Experiments on a gravity-free dispersion of large solid spheres in a Newtonian fluid under shear," Proc. R. Soc. London, Ser. A **255**, 49–63 (1954).
[29] F. Engelund and E. Hansen, *A Monograph on Sediment Transport in Alluvial Streams* (Danish Technical Press, Copenhagen, 1967).

Published under license by AIP Publishing

[30]H. A. Einstein, "The bed-load function for sediment transportation in open channel flows," in *Technical Bulletin* (United States Department of Agriculture, Soil Conservation Service, Washington, DC, USA, 1950), p. 1026.
[31]S. Z. Ali and S. Dey, "Bed particle saltation in turbulent wall-shear flow: A review," Proc. R. Soc. A **475**, 20180824 (2019).
[32]S. Z. Ali and S. Dey, "Hydrodynamics of sediment threshold," Phys. Fluids **28**, 075103 (2016).
[33]S. Dey and S. Z. Ali, "Stochastic mechanics of loose boundary particle transport in turbulent flow," Phys. Fluids **29**, 055103 (2017).
[34]S. Dey and S. Z. Ali, "Mechanics of sediment transport: Particle scale of entrainment to continuum scale of bedload flux," J. Eng. Mech. **143**, 04017127 (2017).
[35]S. Dey and S. Z. Ali, "Review article: Advances in modeling of bed particle entrainment sheared by turbulent flow," Phys. Fluids **30**, 061301 (2018).
[36]S. Dey and S. Z. Ali, "Bed sediment entrainment by streamflow: State of the science," Sedimentology **66**(5), 1449–1485 (2019).
[37]Z. Cao, G. Pender, and J. Meng, "Explicit formulation of the Shields diagram for incipient motion of sediment," J. Hydraul. Eng. **132**, 1097–1099 (2006).
[38]S. Z. Ali and S. Dey, "Hydrodynamic instability of meandering channels," Phys. Fluids **29**, 125107 (2017).
[39]S. E. Coleman and V. I. Nikora, "Exner equation: A continuum approximation of a discrete granular system," Water Resour. Res. **45**, W09421, https://doi.org/10.1029/2008wr007604 (2009).
[40]M. Sekine and G. Parker, "Bed-load transport on transverse slope. I," J. Hydraul. Eng. **118**, 513–535 (1992).
[41]F. Engelund, "Flow and bed topography in channel bends," J. Hydraul. Div. **100**, 1631–1648 (1974).
[42]A. M. Talmon, N. Struiksma, and M. C. L. M. Van Mierlo, "Laboratory measurements of the direction of sediment transport on transverse alluvial-bed slopes," J. Hydraul. Res. **33**, 495–517 (1995).
[43]E. Meyer-Peter and R. Müller, "Formulas for bed-load transport," in *Proceedings of the 2nd Meeting of International Association for Hydraulic Research, Stockholm, Sweden* (IAHR, 1948), Vol. 3, pp. 39–64.
[44]M. Wong and G. Parker, "Reanalysis and correction of bed-load relation of Meyer-Peter and Müller using their own database," J. Hydraul. Eng. **132**, 1159–1168 (2006).
[45]E. W. Lane and A. A. Kalinske, "Engineering calculations of suspended sediment," Trans., Am. Geophys. Union **22**, 603–607 (1941).
[46]J. A. Jiménez and O. S. Madsen, "A simple formula to estimate settling velocity of natural sediments," J. Waterw. Port Coastal Ocean Eng. **129**, 70–78 (2003).

Published under license by AIP Publishing